Characterization of pores in polished low temperature co-fired glass-ceramic composites for optimization of their micromachining

Surface Topography: Metrology and Properties

PAPER

Characterization of pores in polished low temperature co-fired glass-ceramic composites for optimization of their micromachining

Heike Bartsch[1], **Maksim Lubov**[2], **Vladimir Kharlamov**[2], **Juan Jesús Jiménez**[3,4], **Francisco Miguel Morales**[3,4] **and Jörg Pezoldt**[1]

[1] Technische Universität Ilmenau, Institute of Micro-and Nanotechnologies MacroNano, Germany
[2] Alferov University, St. Petersburg, Russia
[3] Institute of Research on Electron Microscopy and Materials IMEYMAT, University of Cádiz, Spain
[4] Department of Materials Science and Metallurgical Engineering and Inorganic Chemistry, Faculty of Sciences, University of Cádiz, Spain

E-mail: heike.bartsch@tu-ilmenau.de

OPEN ACCESS

RECEIVED
1 August 2022

REVISED
30 October 2022

ACCEPTED FOR PUBLICATION
15 November 2022

PUBLISHED
2 December 2022

Keywords: surface analysis, LTCC, polishing, glass-ceramic composite, low temperature co-fired ceramics, laser scanning microscopy, pore analysis

Abstract

Pores are intrinsic defects of ceramic composites and influence their functional properties significantly. Their characterization is therefore a pivotal task in material and process optimization. It is demonstrated that polished section analysis allows for obtaining precise information on pore size, shape, area fraction, and homogeneous distribution. It is proven that laser scanning microscopy provides accurate height maps and is thus an appropriate technique for assessing surface features. Such data is used to compare areas with good and poor polishing results, and various surface parameters are evaluated in terms of their informative value and data processing effort. The material under investigation is a low temperature co-fired ceramic composite. Through statistical analysis of the data, the inclination angle was identified as an appropriate parameter to describe the polishing result. By using masked data, direct conclusions can be drawn about the leveling of load-bearing surface areas, which are crucial in photolithographic processing steps and bonding technology. A broad discussion of different defects based on the results contributes to a critical analysis of the potentials and obstacles of micromachining of low temperature cofired ceramic substrates.

Formula symbols and their meaning

Symbol	Meaning
h	Inhomogeneity factor
ρ, ρ_l	Average (overall) pore density, local one
m	Number of cells along the X and Y axes
n	Number of pores
M	Mesh size
R_{eq}	Equivalent radius for a circle
L_M/l_m	Length of the ellipse major/minor axis
A_{CSp}	Cross-sectional area of pores
A_{CS}	Total image area
η	Pore shape factor
Φ, Φs	Porosity, surface porosity
α	Inclination angle
$S_{exp,th}$	Experimental/theoretical PSD function (fit)
A, B, C	Fit coefficients of the theoretical PSD function
k	Spatial frequency
t	Polishing time
$\sigma_{c,e}$	Surface roughness (center, edge)
$\omega_{c,e}$	Surface waviness (center, edge)
$\lambda_{\sigma,\omega}$	Cut-off wavelength (roughness, waviness)

1. Introduction

Ceramic composite materials are steadily conquering new areas of application, as desired functional properties can be specifically adjusted by combining material properties of matrix and filler in a sophisticated way. So is it for example possible to improve properties such as their mechanical strength [1–3] or energy density [4] and tune parameters like permittivity [5–7] or conductivity [8]. Widely used processes for the synthesis of such composites are spray pyrolysis [8, 9] and powder-based sintering [1, 6, 7, 10, 11] which entail a porous material structure. Low temperature cofired ceramics (LTCC) are a group of glass-ceramic matrix composites that are densified by viscous flow as the major driving mechanism during the sintering process [12]. Co-firing means that conductor lines are printed on ceramic green tapes, and various tapes are stacked and fired in a single process step in order to produce three-dimensional wiring in ceramic circuit carriers [13]. Combining sintering temperatures below 950 °C and tunability of thermo-physical and dielectric properties by varying the glasses and ceramic fillers used allows the modification of functional properties in a wide range and the usage of highly conductive metals as wiring which results in an excellent signal transition [14]. This opens up broad and diverse fields of electronic applications, covering wireless communication [15–17], electromechanical microsystems [18, 19] as well as medical and automotive electronics [20, 21]. Growing demands of integration density, miniaturization, and reliability drive the convergence of this technology towards micromachining. Furthermore, the integration of high-k and low-k materials with defined thickness and low loss tangent is crucial for the realization of the next generation of high-frequency circuits [15, 17]. It has been recently shown that a defined porosification of sintered LTCC by wet chemical etching can be used to tune permittivity [22, 23].Further, porosification depends on the sintering process [24]. Present voids decrease permittivity and loss tangent. The description of such voids or pores as an intrinsic structural feature of ceramic matrix composites is thus essential for understanding the material behavior. However, the characterization of pores, especially of those called 'dead pores' which are fully buried within the solid body, is challenging. Simple methods, such as mercury porosimetry, capillary flow porometry, and gas pycnometry deliver no suitable information regarding these pores. Alternatively, there are non-destructive methods like micro-computer tomography [25, 26] or nuclear magnetic resonance analysis [27], but these methods are expensive and therefore not widely available. Microscopy-based methods using image analysis techniques were already proposed in the past, using scanning electron microscope (SEM) images as the base for pore analysis of LTCC [28], but the necessary preparation using focused ion beam (FIB) is laborious and the region of interest is restricted by the field of view of an SEM image. In this work, we use laser scanning microscopy (LSM) image analysis of polished surfaces to characterize the pores of the composite. The method can detect defects in the range of 10 μm to 100 nm and optimally complements thus classical microscopy and scanning electron microscopy [29]. The measurement delivers two different image types, namely an intensity map and a height map. Considering both sources of information, the uniformity of the pore distribution is evaluated, parameters for an effective surface description are compared and their change depending on polishing progress is assessed.

2. Methods

The data processing is carried out according to the procedure in [30]. Gwydion software [31] is used for image processing.

2.1. Data acquisition

2.1.1. LTCC samples

This work uses a multilayer stack of commercially available LTCC (9k7). The fired single-layer thickness is 100 μm. It is important to mention the single-layer thickness since inhomogeneous particle distribution along the cross-section resulting from the casting process can lead to stratification in the sintered ceramic and cause inhomogeneous pore distribution. The overall thickness of the substrate was 600 μm.

9 k7 consists of ceramic filler (Al_2O_3) and glasses that form different crystalline phases with this filler during sintering. The depleted glass serves as a matrix [32]. This glass matrix provides a closed surface since the filler particles are completely enclosed by the same after sintering. The sintered body has a high form deviation (low-frequency component of surface texture), and the warping can be up to 100 μm. It is made plane-parallel by lapping according to [33]. The substrate has a concave shape after lapping, and the total thickness deviation between the edge region and center is 5 μm, approximately. Lapping eliminates the unevenness but opens the enclosed pores. Figure 1 shows a high-angle annular dark field cross-section image, taken under scanning-transmission electron microscopy mode (STEM-HAADF) of the composite material surface after polishing. A pore is visible at the surface. The surrounding material, consisting of glass and filler, is leveled, but the softer glass shows stronger erosion than the hard filler. Polishing levels the elevations around large pores, but the pores themselves cannot be eliminated, as new ones are opened when others are completely ablated.

2.1.2. Measurement data

The surface data are captured with a laser scanning microscope (LEXT OLS4100, Olympus Corp.) and

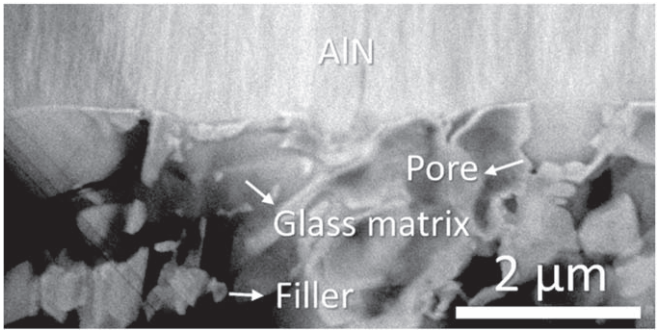

Figure 1. STEM-HAADF cross-section image of a polished LTCC-surface (9k7, DuPont Nemours), revealing the grain and surface structure of the polished LTCC. Typical particle sizes of the alumina filler in the glass matrix are around 1 μm. An AlN layer was sputtered on the LTCC surface to keep it stable during preparation.

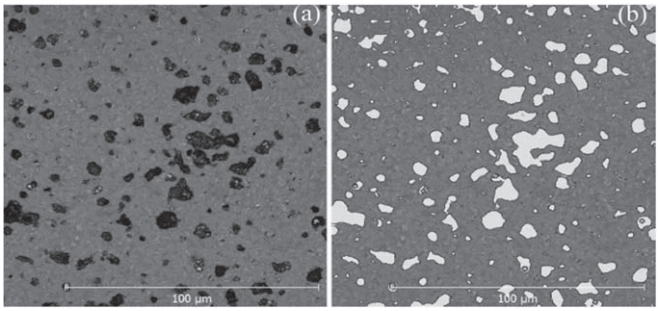

Figure 2. Micrograph of a polished LTCC cross-section, the field of view is 128 μm: (a) untreated intensity image; (b) intensity image with mask (pores are indicated by white color).

contain a complete set of intensity data, and height information depending on the x-y position. These source data are directly imported into the evaluation software. The measurement points are chosen in the center and the edge of the substrate. Due to the concave shape, the polishing results of these regions differ significantly.

2.2. Characterization of the pores

2.2.1. Masking of pore areas

The areas of the pores are extracted from the measurement data. The procedure uses different zero-level definitions for cross-sectional images and in-plane images since the protruding surface differs significantly with increasing polishing progress. Figure 2(a) shows the raw intensity data and figure 2(b) depicts the masked pore area.

The unmasked areas are the load-bearing regions of the surface and thus representative of the contact of a lithography mask, the adhesive area for chip bonding, or the effective area of a metallization.

2.2.2. Pore distribution homogeneity

The inhomogeneity of the pores is calculated using the inhomogeneity factor h [7, 34]. The spatial distribution of the respective central point of the pore is used. The method is based on the calculation of the deviation of the local pore density ρ_l from the value of the average (expected) pore density ρ, which corresponds to the number of pores n per cross-section divided by the cross-sectional area of the sample. Figure 3 gives an example of three point distributions and associated inhomogeneity values according to [34].

To calculate the local pore density ρ_l, the entire surface is first divided by a mesh into m^2 rectangular cells of equal area, and then the ratio between the number of pores n in each cell and the cell area is calculated for each cell. The value of the local density in this case depends on the cell size and the offset (x,y) between the beginning of the mesh and the surface boundaries. The inhomogeneity factor $h(x,y)(m)$ for the given partition m and offset (x,y) is given by:

$$h_{(x,y)}(m) = \frac{1}{2n}\sum_{i=1}^{m^2}|\rho_l - \rho| \tag{1}$$

By varying the offset, we can find the maximum value $h(m)$ [34]:

$$h\,(m) = \frac{1}{2n}\max_{(x,\,y)}\sum_{i=1}^{m^2}|\rho_l - \rho| \tag{2}$$

The inhomogeneity factor h should not depend on the mesh size, so it is calculated as a weighted sum of inhomogeneity factors for a set of given partitions $m = 1..M$:

Figure 3. Examples of different inhomogeneity values [34] (reprint with permission from IEEE).

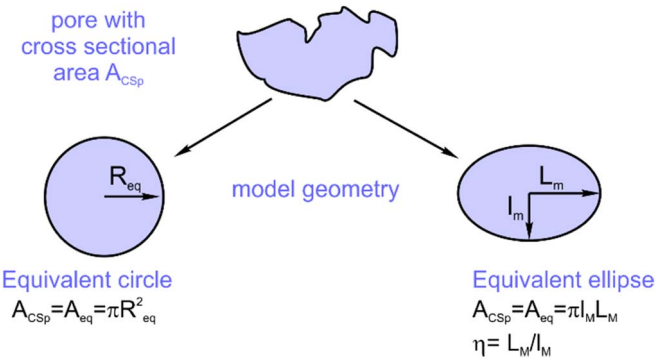

Figure 4. Model geometries for the pore cross-section. The equivalent circle has the same area as the pore cross-section. The equivalent ellipse additionally has the same area distribution. R_{eq} is the radius of the equivalent circle, L_M and lm are the lengths of the major and minor axes of the equivalent ellipse, respectively.

$$h = \sum_{r=1}^{M} w^{1-r} h(m) \tag{3}$$

$$h = \frac{1}{2n} \sum_{m=1}^{M} w^{1-m} \max_{(x,y)} \sum_{i=1}^{m^2} |\rho_l - \rho| \tag{4}$$

The value of the weighted coefficient w is estimated to be 4.79 according to [34].

The h factor has a value range of 0–1, where 0 corresponds to an ideal, uniform distribution and 1 to an inhomogeneous one. The experimental determination of the pore distribution is based on 6 measurement points which are randomly distributed along the cross-sections of the LTCC substrate. The field of view of a single image is 256 μm × 256 μm and comprises thus at least two individual layers of fired ceramic. A process-related pore layering (stratification) would therefore lead to a significant inhomogeneity in the images. The used algorithm is provided in [35].

2.2.3. Pore shape factor

The complex pore shapes must be described by simplified models. The most obvious way is to describe the intersection surface of the pore by a circle with an equivalent radius R_{eq}. A more accurate approximation is provided by the ellipse since this model allows to capture anisotropic geometries of the cross-sectional area of the pore A_{CSp}. Figure 4 illustrates both models.

While for the equivalent circular model the equality of the surfaces serves as the basis for calculation, for the description of the equivalent ellipse a second parameter is required to determine the ratio η of major to minor axis L_M and l_m. Here, the moment of inertia of the surface is used, which has the same value for a real pore and ellipse surface area. The ratio η is called the pore shape factor in this work.

The measured height data are used to determine the pore height distribution. It should be mentioned here that a systematic error results from the fact that the undercut of inclined pores cannot be detected by the measurement procedure. In this case, the actual depth is greater than the measured depth.

2.2.4. Porosity

The porosity Φ is defined as the proportion of the volume of the voids V_p, in the total volume V [36]. The surface porosity Φ_s which can be determined on the basis of two-dimensional images corresponds to the relation between the sum of the area A_{CSp} of all pores as a direct result of image evaluation and the total area of the cross-section A_{CS}, which is equal to the image size of 256 μm × 256 μm.

$$\phi_S = \frac{\sum A_{CSp}}{A_{CS}} \tag{5}$$

Since we can assume a uniform pore distribution in the volume, this two-dimensional ratio is transferred into a volume ratio by replacing each surface element with a volume element. The resulting porosity Φ is:

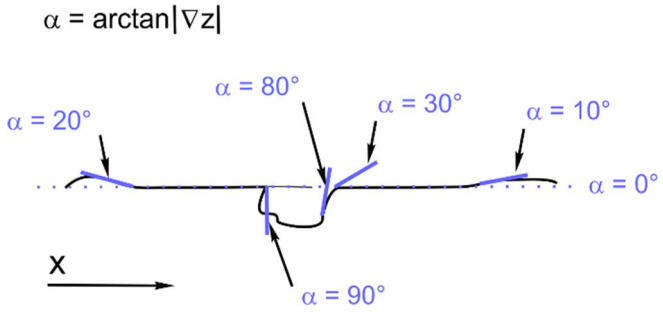

Figure 5. Illustration of the inclination angle obtained as a function of topography data. The inclination angle α has a value range from 0° to 90° since the absolute value is considered.

$$\phi = \phi_s^{\frac{3}{2}} \tag{6}$$

2.3. Statistical analysis for assessment of the polishing process

2.3.1. Analysis of the height distribution

For a better understanding of the polishing process, the height distribution of the measured values is examined using masked data. Details of the masking procedure can be found in [30]. It separates the height data depending on their location inside and outside the pore surface. The assigned distribution functions f_z are presented for different polishing times.

2.3.2. Analysis of the inclination angle

The inclination angle α represents the slope of the surface features. It results from the partial derivation of the height data z using the del operator ∇. Figure 5 illustrates typical values of α for different surface slope configurations.

A zero-degree angle represents a flat surface and large angles represent steep surface features, such as those found on pores. Undercut cannot be detected. If this is the case, the result is an angle of 90°.

2.3.3. Spectral power density analysis (PSD)

The spectral power density (PSD) function S represents the height distribution of surface structures as a function of spatial frequencies k, which is the reciprocal of the lateral size of the surface structure. The one-dimensional PSD function S can be calculated from surface height data $z(x)$, where x is the one-dimensional coordinate, and k is the spatial frequency [37]:

$$S = \frac{1}{L}\left|\int_0^L z(x)e^{-2\pi ikx}dx\right|^2 \tag{7}$$

L is the size of the scan. The unit of S is [μm^3]. The experimental function S_{exp} is now assumed to be the sum of a number of superposed theoretical functions S_{th} that can be described by an ABC-model (S_{ABC}) which is extensively used in PSD analysis [38]:

$$S_{ABC} = \frac{A}{(1+(Bf_x)^2)^{\frac{C}{2}}} \tag{8}$$

$$S_{th} = S_{ABC1} + S_{ABC2} \tag{9}$$

The PSD function is a suitable tool to extract different types of surface deviations, e.g. roughness and waviness or periodic superstructures, from the surface topography. By analyzing them, it is possible to assess which structural quantities occur frequently and whether periodic structures are present on the surface. They appear as peaks in the diagram of the PSD function.

2.3.4. Root mean square height analysis

The root mean square (RMS) value is a widely used surface parameter. A detailed surface analysis requires the representation of surface topography as the sum of three components, namely roughness, waviness, and shape [39]. These contributions to topography have different lateral dimensions. The shape contribution was eliminated by aligning the height data to the mean reference plane. Since the topographic features of large pores differ significantly from those of the polished surface, the corresponding data are extracted by the masking process [30] and are not included in the analysis.

Since the polishing process mainly levels the load-bearing areas outside the pores, their surface data are removed by masking and are not included in the consideration. A zero-order Gaussian regression filter (ISO 16610-71) is therefore applied to the remaining height data.

The cutoff wavelengths $\lambda_{\sigma,\omega}$ are obtained as the reciprocal of the respective cutoff frequency in the PSD function (section 3.2.3 PSD). The values were chosen so that the cutoff frequency of the waviness is smaller than all k_1 values and the cutoff frequency for the roughness is larger than all k_2 values. λ_σ is consequently 1 μm and λ_ω 3 μm.

3. Results

3.1. Pore analysis of cross-sectional images

3.1.1. Homogeneity of pore distribution and porosity

The investigation of this pore distribution provides information on whether the layered character of the LTCC substrate leads to stratified pore formation in

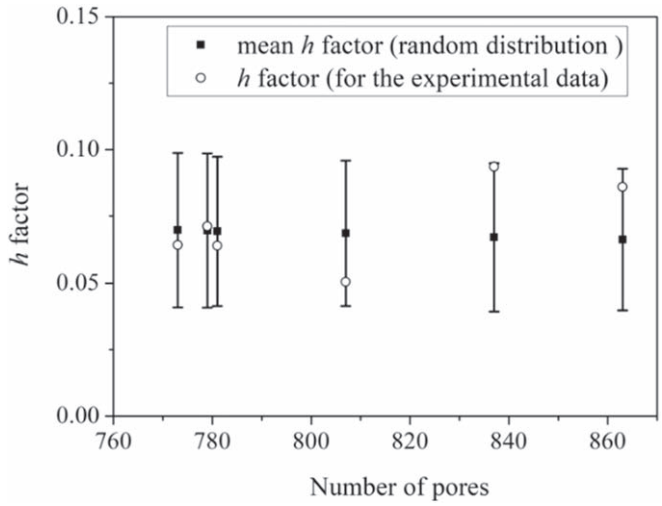

Figure 6. Comparison of mean *h* factor for the random distributions and h factor for the experimental pore distributions extracted from the cross sections. Deviation for the mean h factor is equal to +/- three standard deviation values.

the sinter body. The total number of pores in the images varies from 773 to 863. The experimental homogeneity values are compared with a reference value obtained by applying the same procedure on a set of randomly distributed model pores. The Monte Carlo method is used to generate a set of 1000 uniform spatial distributed model pores [40]. Figure 6 depicts the experimental and reference data for comparison.

All the means of the experimental h values are smaller than 0.1 indicating a nearly homogenous pore distribution. All of them are in the range of three times the standard deviation of the random data. Consequently, no significant stratification of the pore distribution can be identified.

The surface porosity Φs of the cross-section micrographs of the bulk LTCC varies between 9.5 to 13% for six available measurements. The corresponding porosity Φ according to equation (6) amounts to 3.0 to 4.7%.

3.1.2. Pore size and shape

The R_{eq} value is a direct measure of the lateral size of the pores and the open pore area. Figure 7(a) depicts its distribution in blue and the related total area of pores for discrete R_{eq} values in red. We observe a skewed distribution, the median value $\widetilde{R_{eq}}$ is equal to 1.0 μm and the mean value $\overline{R_{eq}}$ is equal to 1.35 μm. The area distribution has an almost symmetric shape. The total area of the most abundant small pores contributes only to a small amount to the open area. Pores with R_{eq} in the range of 2–4 μm contribute the most.

The skewed distribution of R_{eq} can be explained by the presence of two superposed pore sizes of a bimodal distribution. Figure 7(b) shows the fitting curves of the distributions with bins size obtained using Scott´s normal reference rule. The median of normal distribution 1 (green curve), $\widetilde{R_{eq}}^{1}$ is 0.56 μm and $\overline{R_{eq}}^{1}$ is 1.04 μm. For normal distribution 2, (red) $\widetilde{R_{eq}}^{2}$ is 1.46 μm and the $\overline{R_{eq}}^{2}$ is 1.67 μm.

The observation of two different pore distributions raises the question of whether there are different mechanisms behind them, which can be distinguished by the shape of the pores. Therefore, the distribution function of the pore shape factor was separately evaluated for all of them, i.e. (f_t), small pores (f_s), and large ones (f_l). The classification in small and large pores uses the mean value $\overline{R_{eq}}$ as the separation criterion, meaning that those pores with larger R_{eq} are assigned to the distribution function of the large and smaller ones to the small, accordingly. Figure 8 depicts the results.

All the distribution functions have maxima at similar values of the shape factor. Deviations in counts are a consequence of the different total number of pores. The jumps on the red curve near integer values of η are artifacts due to the discrete number of pixels contributing to the spot size for small pores. These jumps are also clearly visible on the curve for all pores since small pores are predominant in number. The respective values for $\bar{\eta}$ are 1.75 for all, 1.74 for small, and 1.76 for large pores. The median $\tilde{\eta}$ is 1.55 for all, 1.54 for small, and 1.58 for large pores. This comparison leads to the assumption that the pore shape is independent of the pore size.

3.2. Parameter for polishing assessment

The polishing progress is compared at two substrate points. The concave shape of the substrate results in the edge areas being smoothed out, while the center of the substrate is not polished beyond a certain degree of removal. Thus, the edge area can serve as an example of a good polishing result, while the central area serves as an example of a poorly polishing result.

3.2.1. Comparison of pore characteristics

The pore characteristics in-plane for the different polishing steps are compared with those of the cross-

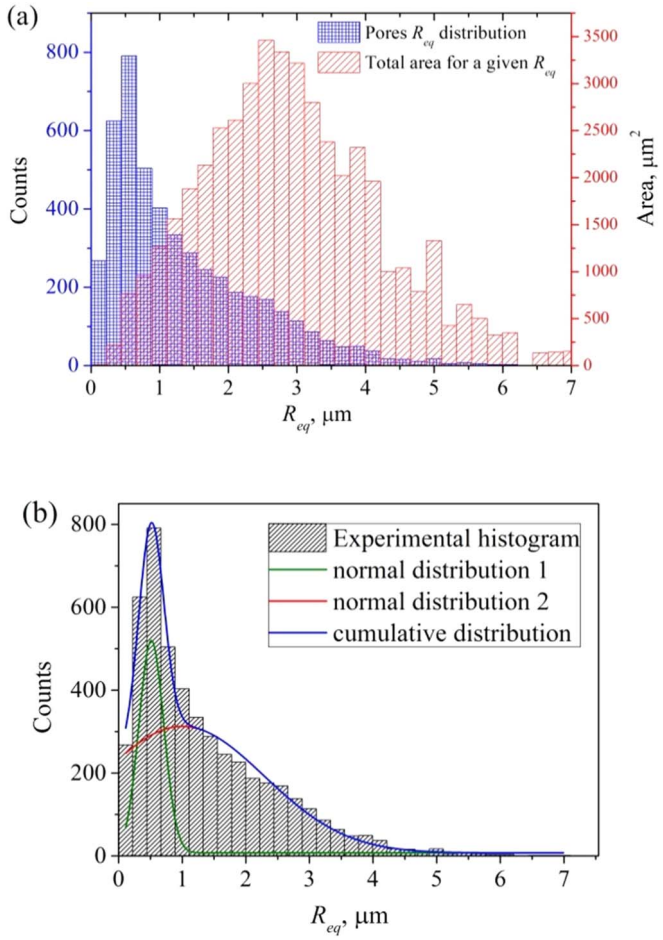

Figure 7. (a) Pores equivalent radii and total area for given equivalent radius distributions and (b) fit of 2 superposing distribution curves.

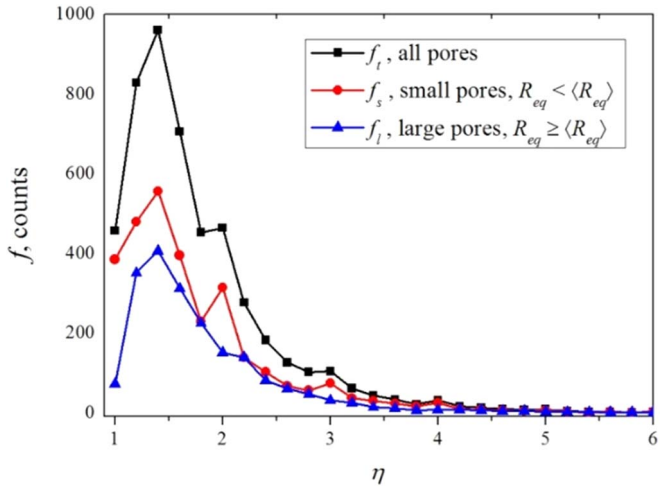

Figure 8. Pores shape factors distributions for various ranges of R_{eq}.

sectional ones. Since the surface qualities differ considerably between the finely polished cross-sectional area and the in-plane ones, particularly a after short polishing time, only reference pores with a depth of less than 600 nm are included in the consideration. This value corresponds approximately to the leveled height during polishing. The results are summarized in table 1.

Pore size and pore shape are similar. The mean value of the pore size .. of cross-sectional pores is a bit

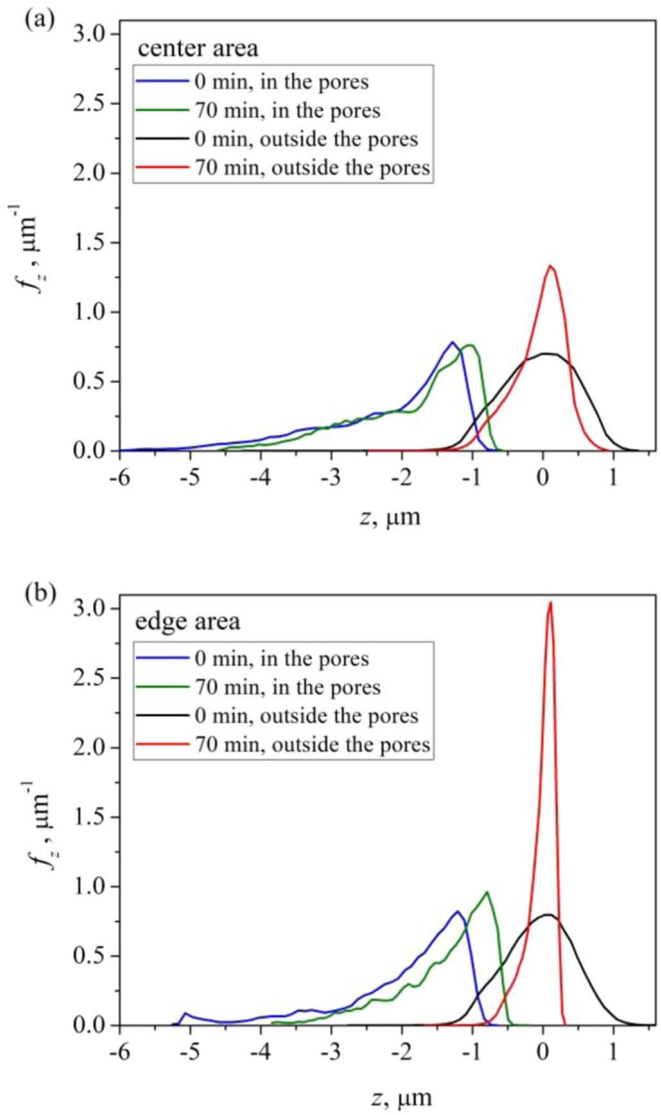

Figure 9. Height distribution functions f_z for central area (a) and for the left upper corner (b) before polishing (0 min) and after 70 min polishing.

Table 1. Pores characteristics for different polishing times at the center area, compared with reference pores of the cross-section.

Polishing time [min]	*h* factor	$\overline{R_{eq}}$ [μm]	$\bar{\eta}$	$\tilde{\eta}$
0	0.183	1.96	1.72	1.58
20	0.150	1.96	1.61	1.45
50	0.152	1.78	1.83	1.6
70	0.177	1.9	1.67	1.52
Reference	0.157	2.14	1.71	1.51

higher than those of the in-plane values. This can be a random effect, but a systematic influence of the masking cannot be excluded due to the different surface qualities.

3.2.2. Evolution of the surface height and slope distributions

The presentation of the surface height distribution functions f_z considers the data points of the masked (in the pore) area and the surrounding data points (outside the pores) separately. Figure 9 compares the respective functions for the data sets in the beginning and after completion of the polishing step for the well-polished edge area and the poor-polished center area. The zero level is defined as the peak of the Gaussian distribution of the values outside the pores.

The height distribution functions of the values inside the pores show no significant change in their shape, but for both regions, the center and the edge, a parallel shift to higher z values with increasing polishing time is evident.

The data sets outside the pores provide essential information on the erosion of the raised surface structures. While the distribution functions of the center and edge regions are initially comparable, they differ substantially after polishing. The well-polished edge area shows a narrow and high peak, which is flattened. The flattened flank is the result of leveling the protruding ridges during polishing that generates a large

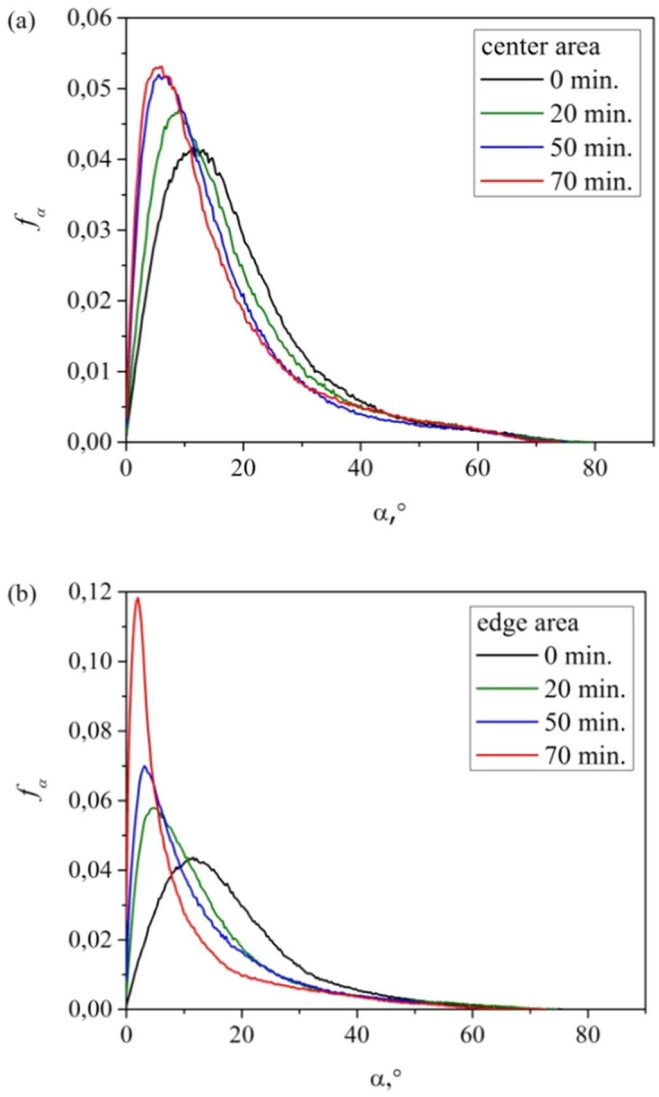

Figure 10. Inclination angle distribution functions for the central area (a) and for the left upper corner area (b) of the sample surface with different polishing times.

number of data points with the same height. Since the poor polishing condition in the center produces only limited leveling, the distribution here is broader and more symmetrical because of the remaining hill stumps.

The distribution function of the inclination angle f_a bases on the full set of height data for the respective polishing step. Figure 10 depicts the functions for the center and the edge area at different polishing times.

Figure 5 illustrates that small inclination angles imply a flat surface. A good polishing result is therefore associated with a high proportion of small angles and a narrow distribution.

The curves in figure 10(a) develop towards a lower inclination angle and higher peaks with an increasing polishing time of up to 50 min. However, there is no significant change between the curves at 50 min and 70 min, indicating that there is no more polishing progress. The situation is different in figure 10(b): peak height and width change over the whole time, the 70-min-curve has an almost double peak value than the 50-min one and the peak width is narrow, indicating apparent progress in polishing between 50 min and 70 min.

3.2.3. Evaluation of the PSD function

The PSD functions of the center area before polishing and the edge area after polishing are taken as representative examples of the worst and the best polishing result, respectively. The experimental curves S_{exp} are approximated by the theoretical S_{th} values that can be fitted by two analytical functions S_{ABC1} and S_{ABC2} (referend as theoretical function in figure 11). The respective coefficients for both polishing states are summarized in table 2.

Two functions with spatial low-pass behavior superpose each other. ABC1 represents the curve with the higher spatial cutoff frequency and ABC2 is the one with the lower one.

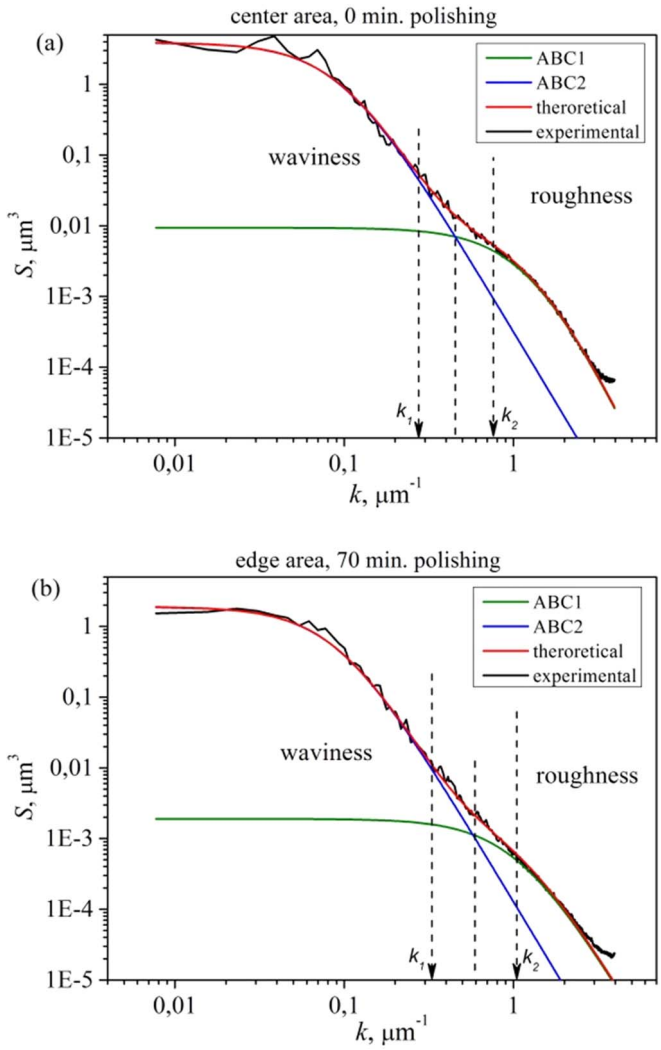

Figure 11. S_{exp} (black line) and S_{th} (red) as a sum of two analytical PSD functions (ABC1, ABC2) for a) a center area before polishing t = 0 min; and b) edge area after polishing, t = 70 min.

Table 2. Fitting parameter of the ABC functions for an unpolished (center) and well-polished polished (edge) surface.

	Center, 0 min		Edge, 70 min	
	ABC1	ABC2	ABC1	ABC2
A [μm^3]	0.0094	3.9	0.0019	1.9
B [μm]	0.78	10.5	0.941	11.01
C	5	5	4	4

Figure 11 illustrates that the analytical functions are shifted towards higher spatial frequencies with increasing polishing progress. The frequencies k_1 and k_2 divide the spatial frequency range into three regions: (i) low-frequency region, $k < k_1$; (ii) transition region $k_1 < k < k_2$; and (iii) high-frequency region, $k > k_2$. The values $k_{1,2}$ are shown here graphically, the modeling is presented in the supplement [30]. The low-frequency region characterizes the waviness of the LTCC substrate, whereas the high-frequency region is determined by the RMS roughness.

3.2.4. Roughness and waviness evolution

Separating roughness and waviness from the primary surface allows the study of coarse and fine surface features individually. Figure 12 compares the RMS height for roughness and waviness according to the substrate position.

Both roughness and waviness decrease differently over the polishing time depending on the substrate position. While there is no significant decrease in roughness and waviness in the center area after 50 min polishing time, the edge area is still leveled and both roughness and waviness decrease between 50 min and 70 min The results correlate well with those in figures 9 and 10 in section 3.2.2.

The machining process affects the various spatial sizes to different extents. The final roughness of the well-polished surface is 42 nm. This corresponds to 47% of the initial value. The coarser structures, typified by waviness, reach an RMS height of 137 μm, which is 32% of the initial value. Coarser structures are thus eroded more strongly.

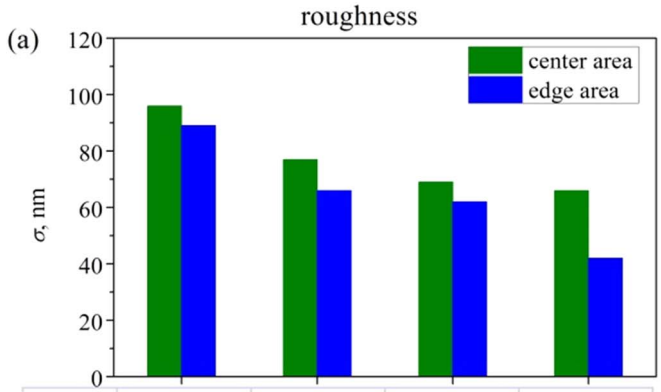

t, min	0	20	50	70
σ_c, nm	96	77	69	66
σ_e, nm	89	66	62	42

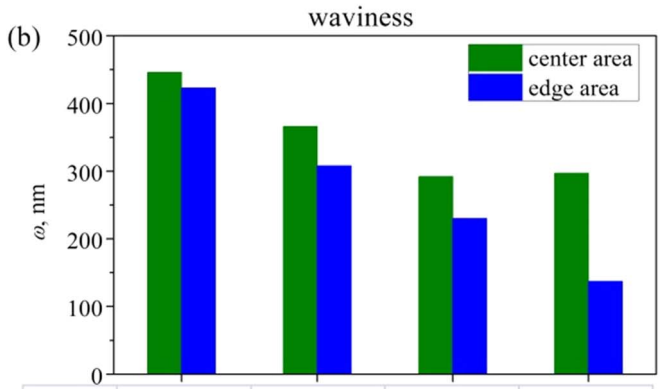

t, min	0	20	50	70
ω_c, nm	446	366	292	297
ω_e, nm	423	308	230	137

Figure 12. RMS of surface roughness and waviness after different polishing time t, filtered with a robust zero order areal Gaussian filter (ISO 16610-61): (a) RMS roughness for center σ_c and edge σ_e, $\lambda_\sigma = 1$ μm; (b) RMS waviness for center ω_c and edge ω_e areas, $\lambda_\omega = 3$ μm.

4. Discussion

4.1. Pore distribution and shape

The results in figure 6 reveal that there is no stratification due to the process and that the pores are evenly distributed over the cross-section. Comparing these results with table 1, it is noticeable that the results differ considerably. Although the data set is the same, the analysis of the reference pores yields deviating values. The reason for this lies in the selection and processing of the data. Since only larger pores are considered in table 1, the total sample size, which corresponds to the number of pores, is lower. Additionally, the pores are represented by a point that is situated in the center of the equivalent circle. If the pore area is large, no other pore can be located within its circumference. Both reasons cause a shift of the h-value towards larger values. However, the h-values for the cross-section and those of the planes do not differ significantly, therefore a homogeneous distribution of the pores in the volume is confirmed by this evaluation.

A correlation between polishing depth and pore density was not found.

The shape factor η can indicate if there exist process-related deformations of the pores, e.g., due to the escape of gases to the top. In this case, there would be a smaller shape factor in-plane than perpendicular to the polishing plane. Actually, a slightly higher shape factor was observed for cross-sectional pores in comparison to the in-plane. Since the effect is small in comparison to the standard error, the observation can be random. A systematic influence of the masking cannot be excluded too, due to the different surface qualities. Based on the available data, no reliable statement can be made, and further studies are required.

4.2. Assessment of polishing progress

4.2.1. Use of distribution functions

Both, the height and the inclination angle distribution function are suitable for describing the polishing progress. In the case of the height distribution, the peak height, width, and shape of the data point distribution outside the pores are considered quality characteristics since they allow us to clearly distinguish between good and bad polishing results. However, the use of the inclination angle appears to be easier to realize, since here peak height and width can be determined from the total data set and no masking is required.

4.2.2. RMS height values

RMS height values for roughness and waviness are qualitative target values that can be directly brought in relation to process requirements. Applying a PSD analysis helps to identify the cut-off wavelength for standard filters. Waviness and roughness differ significantly depending on the degree of polishing and in the case of poor polishing, a clear saturation effect is identified, indicating that the erosion does not proceed in the center area of the substrate after 50 min. RMS height values for waviness allow the evaluation of the bearing surfaces on which a lithography mask would have direct contact during light exposure. This allows the light scattering at the gaps to be estimated. The RMS roughness itself is of particular interest for the assessment of the sheet resistance, e.g. the adhesion of bond connections.

4.3. Limiting aspects for micromachining

The use of micromachining makes sense if the desired function cannot be achieved with thick-film technologies. For conductive tracks as the most important functional units of a circuit, the limit of feasible printed structures is approximately 50 μm. A reasonable target range for the width of thin film conductors to complement LTCC technology is therefore in the interval of 5–25 μm.

According to figure 7(a), R_{eq} of most pores is smaller than 1 μm. A conductor path would therefore not be interrupted when crossing these pores, but its current-carrying capacity would decrease significantly due to the cross-section reduction. Furthermore, the resulting defects can generate electromagnetic radiation, since they represent a discontinuity in wave propagation. Although this pore class is the most abundant, its percentage of the substrate area and thus the probability that they interrupt a conductor path fully is relatively low.

The highest risk originates from pores of size between 2–4 μm. Due to their size, they would significantly constrict or even completely interrupt conductor paths. Even larger pores are rare, but they almost certainly lead to a failure of the structures and thus limit the yield.

Another criterion for assessing the transmission quality of thin-film conductor lines is sheet resistance. It increases with increasing roughness. This impairs the transmission quality of signals, especially in the high-frequency range. The achieved surface roughness of 42 nm is of the order of that achieved by sol-gel coatings of LTCC surfaces. Here, R_a is 45 nm, and the increase in sheet resistance of a copper conductor due to this roughness is increased by a factor of 1.7 compared to a silicon substrate [41]. A similar ratio is expected for metallizations on polished surfaces.

The waviness of well-polished surfaces is 137 nm and the roughness is 42 nm. The polishing process thus produces surfaces with optical quality. In the lithography process, the waviness can be considered as the average gap that remains when exposed in hard contact mode, provided that the substrate is flat enough and shape deviations are corrected by the contact force. Assuming a structure size of 5 μm and more, good exposure conditions can be assumed under these conditions.

5. Conclusion

LSM image analysis was applied to characterize pores as major surface defects of polished LTCC ceramics. It was found that the pores are homogeneously distributed in the volume and that those with a radius R_{eq} smaller than 1 μm are the most abundant, but their contribution to surface defects is minor. Pores with an equivalent radius R_{eq} of 2 to 4 μm represent the largest proportion of defects in terms of area. It is demonstrated that the polishing progress can be evaluated by analyzing the distribution function of the inclination angle, taking into account only the peak height and width of the unmasked data. This approach is well-suited for automated quality assessment. The results of the statistical pore analysis are comparable to the progression of the RMS values. It is demonstrated that both methods confirm the same statement. Since the developed statistical pore analysis method is independent of the material, it can be applied to characterizing pores in various ceramic composites and providing information on porosity, pore size, shape, and distribution. These methods pave the way for improved process control and help to assess the micromachining compliance of ceramic substrates.

Data availability statement

The data that support the findings of this study are openly available at the following URL/DOI: https://doi.org/10.5061/dryad.kwh70rz5w.

Funding

The authors acknowledge the support of this research by the program of the Carl-Zeiss-Stiftung, program

'Durchbrüche' by the project 'MemWerk' under contract P2018-01-002 and DAAD under grant 57435564. Further, the support by the Center of Micro- and Nanotechnologies (ZMN) (DFG RIsources reference: RI_00009), a DFG-funded core facility (Grant No. MU 3171/2-1 + 6-1, SCHA 632/19-1 + 27-1, HO 2284/4-1 + 12-1) of the TU Ilmenau, is gratefully acknowledged. The work of J.J. Jiménez and F M Morales was partially supported by the University of Cádiz through the 'Programa de ayudas a la realización de Tesis Doctoral del Plan Propio de Investigación y Transferencia' (Contratos predoctorales de Formación de Profesorado Universitario (fpuUCA) 2016-060/PU/EPIF-FPU-CT/CP). They also wish to acknowledge the IMEYMAT Institute for its support by granting a 'Líneas Prioritarias' project (ref. PLP2020120-1).

Conflict of interest

All authors declare that they have no conflicts of interest.

ORCID iDs

Heike Bartsch https://orcid.org/0000-0001-7199-7600
Maksim Lubov https://orcid.org/0000-0002-8020-9458
Vladimir Kharlamov https://orcid.org/0000-0001-8648-4429
Juan Jesús Jiménez https://orcid.org/0000-0003-4303-3083
Francisco Miguel Morales https://orcid.org/0000-0002-8341-2478
Jörg Pezoldt https://orcid.org/0000-0002-2611-7720

References

[1] Yang H *et al* 2021 Effect of graphene on microstructure and mechanical properties of Si_3N_4/SiC ceramics *ES Mater Manuf* **12** 29–34
[2] Zhang H *et al* 2021 Correlation of C/C preform density and microstructure and mechanical properties of C/C-ZrC-based ultra-high-temperature ceramic matrix composites *Adv Compos Hybrid Mater* **4** 743–50
[3] Yan H, Li Q, Wang Z, Wu H, Wu Y and Cheng X 2021 Effect of different sintering additives on the microstructure, phase compositions and mechanical properties of Si_3N_4/SiC ceramics *ES Mater Manuf* **15** 65–71
[4] Ma R *et al* 2022 Enhanced energy storage of lead-free mixed oxide core double-shell barium strontium zirconate titanate@magnesium aluminate@zinc oxide-boron trioxide-silica ceramic nanocomposites *Adv Compos Hybrid Mater* **5** 1477–89
[5] Sun Z, Huang X, Xia A, Yan Z and Qian L 2021 Tunable bandwidth of negative permittivity from graphene-silicon carbide ceramics *Eng. Sci.* **16** 19–25
[6] Dwivedi A, Singh K N, Hait M and Bajpai P K 2022 Ferroelectric relaxor behavior and dielectric relaxation in strontium barium niobate—A lead-free relaxor ceramic material *Eng. Sci.* **20** 117–24
[7] Wu F-F *et al* 2022 Design and fabrication of a c-band dielectric resonator antenna with novel temperature-stable $Ce(Nb_{1-x}V_x)NbO_4$ (x = 0-0.4) microwave ceramics *ACS Appl. Mater. Interfaces* **14** 48897–906
[8] Gao S *et al* 2022 Highly transmitted silver nanowires-SWCNTs conductive flexible film by nested density structure and aluminum-doped zinc oxide capping layer for flexible amorphous silicon solar cells *J Materials Science & Technology* **126** 152–60
[9] Roy R, Das D and Rout P K 2022 A Review of advanced mullite ceramics *Eng. Sci.* **18** 20–30
[10] Ji J, Wang X, Yu J, Li Q, Wang Z and Shi G 2022 Microstructures and mechanical properties of Ti_3SiC_2/Al_2O_3 and Ti_3SiC_2-TiC/Al_2O_3 composite ceramics by modifying Al_2O_3 content via *in situ* synthesized *ES Mater & Manufact* (https://doi.org/10.30919/esmm5f749)
[11] Shi Y, Song X, Han X, Zhang M and Dong M 2021 Influences of additives on crystal multiformity and composition in a CaO–Al_2O_3–MgO–SiO_2–based glass–ceramics *Adv Compos Hybrid Mater* **4** 614–28
[12] Kemethmüller S, Hagymasi M, Stiegelschmitt A and Roosen A 2007 Viscous flow as the driving force for the densification of low-temperature co-fired ceramics *J. Am. Ceram. Soc.* **90** 64–70
[13] Gongora-Rubio M R, Espinoza-Vallejos P, Sola-Laguna L and Santiago-Avilés J J 2001 Overview of low temperature co-fired ceramics tape technology for meso-system technology (MsST) *Sens Actuators A: Physical.* **89** 222–41
[14] Sebastian M T and Jantunen H 2008 Low loss dielectric materials for LTCC applications: a review *Int. Mater. Rev.* **53** 57–90
[15] Watanabe A O, Ali M, Sayeed S Y B, Tummala R R and Pulugurtha M R 2021 A Review of 5G front-end systems package integration *IEEE Trans Compon, Packag Manufact Technol* **11** 118–33
[16] Jantunen H, Kangasvieri T, Vähäkangas J and Leppävuori S 2003 Design aspects of microwave components with LTCC technique *J. Eur. Ceram. Soc.* **23** 2541–8
[17] Ohsato H *et al* 2019 Micro/millimeter-wave dielectric indialite/cordierite glass-ceramics applied as LTCC and direct casting substrates: current status and prospects *J Korean Ceram Soc* **56** 526–33
[18] Jurków D *et al* 2015 Overview on low temperature co-fired ceramic sensors *Sens Actuators A: Physical* **233** 125–46
[19] Jaziri N, Boughamoura A, Müller J, Mezghani B, Tounsi F and Ismail M 2020 A comprehensive review of thermoelectric generators: technologies and common applications *Energy Reports* **6** 264–87
[20] Ciobanu R, Schreiner C, Drug V, Schreiner T and Antal D 2015 Sensors in LTCC-technology with embedded microfluidic features, for medical applications *2015 IEEE Int. Symp. on Medical Measurements and Applications (MeMeA) Proc. (Torino, Italy)* 407–10
[21] Sickinger F, Weissbrodt E and Vossiek M 2018 '76–81 GHz LTCC antenna for an automotive miniature radar frontend,' *Int J Microw Wireless Technol* **10** 729–36
[22] Hajian A *et al* 2019 Wet-chemical porosification of LTCC substrates: dissolution mechanism and mechanical properties *Microporous Mesoporous Mater.* **288** 109593
[23] Steinhäußer F, Talai A, Weigel R, Koelpin A, Bittner A and Schmid U 2016 Permittivity reduction and surface modification by porosification of LTCC *Ceram. Int.* **42** 8925–31
[24] Hajian A *et al* 2022 Impact of sintering temperature on phase composition, microstructure, and porosification behavior of LTCC substrates *J. Eur. Ceram. Soc.* **42** 5789–800
[25] Bertoldi S, Farè S and Tanzi M C 2011 Assessment of scaffold porosity: the new route of micro-CT *Journal of applied biomaterials & biomechanics: JABB* **9** 165–75
[26] Liu Y, Xie D, Zhou R and Zhang Y 2021 3D X-ray micro-computed tomography imaging for the microarchitecture evaluation of porous metallic implants and scaffolds *Micron* **142** 102994

[27] Rezaeizadeh M, Hajiabadi S H, Aghaei H and Blunt M J 2021 Pore-scale analysis of formation damage; A review of existing digital and analytical approaches *Adv. Colloid Interface Sci.* **288** 102345
[28] Steinhäußer F *et al* 2014 Graphical based characterisation and modelling of material gradients in porosified LTCC *J. Eur. Ceram. Soc.* **34** 2833–8
[29] Khafagy K H, Datta S and Chattopadhyay A 2021 Multiscale characterization and representation of variability in ceramic matrix composites *J Composite Mater* **55** 2431–41
[30] Lubov M, Kharlamov V and Bartsch H 2022 Surface measurement data of polished LTCC
[31] Nečas D and Klapetek P 2022 *GWYDDION: Scanning probe microscopy data visualization and analysis* Czech Metrology Institute, Department of Nanometrology http://gwyddion.net/
[32] Dai S 2012 Densification and crystallization in crystallizable low temperature co-fired ceramics *J. Mater. Sci.* **47** 4579–84
[33] Nam G, Michael F, Heike B and Jens M 2015 Lapping and polishing of different LTCC substrates for thin film applications *2015 European Microelectronics Packaging Conf. (EMPC)* pp 1–4 https://ieeexplore.ieee.org/document/7390691
[34] Schilcher U, Gyarmati M, Bettstetter C, Chung Y W and Kim Y H 2008 Measuring Inhomogeneity in Spatial Distributions *VTC Spring 2008 - IEEE Vehicular Technology Conf. (Marina Bay, Singapore)* 2690–4
[35] Lubov M and Kharlamov V 2022 *Pores inhomogeneity measure*. [Online]. Available: https://github.com/modellingioffe/pores_inhomogeneity
[36] Rice R W 1993 Evaluating porosity parameters for porosity-property relations *J American Ceramic Society* **76** 1801–8
[37] Church E L, Takacs P Z and Leonard T A 1989 The Prediction of BRDFs From Surface Profile Measurements *Proc. SPIE 1165 Scatter from Optical Components* 1165
[38] Senthilkumar M, Sahoo N K, Thakur S and Tokas R B 2005 Characterization of microroughness parameters in gadolinium oxide thin films: a study based on extended power spectral density analyses *Appl. Surf. Sci.* **252** 1608–19
[39] Raja J, Muralikrishnan B and Fu S 2002 Recent advances in separation of roughness, waviness and form *Prec Eng* **26** 222–35
[40] Rubinstein R Y and Kroese D P 2016 *Simulation and the Monte Carlo Method* Wiley) (Newark: 3rd edn (https://doi.org/10.1002/9781118631980)
[41] Bartsch H, Brokmann U, Goj B, Weiss R, Rädlein E and Müller J 2015 Sol gel thin films on LTCC ceramic multilayers enable their use as thin film substrates *2015 European Microelectronics Packaging Conf. (EMPC)* pp 1–6